The definitive publisher version is available online at 10.1016/j.mtnano.2022.100200

Ultrafast hydrogenation of magnesium enabled by tetragonal ZrO_2 hierarchical nanoparticles

Xuelian Zhang[a,†], Xin Zhang[a,†], Lingchao Zhang[a], Zhenguo Huang[b], Fang Fang[c]*, Jianjiang Hu[d]*, Yaxiong Yang[e], Mingxia Gao[a], Hongge Pan[a,e], Yongfeng Liu[a,e]*

[a]State Key Laboratory of Silicon Materials and School of Materials Science and Engineering, Zhejiang University, Hangzhou 310027, China

[b]School of Civil & Environmental Engineering, University of Technology Sydney, 81 Broadway, Ultimo, NSW, 2007, Australia.

[c]Department of Materials Science, Fudan University, Shanghai, 200433 China.

[d]School of Chemistry and Chemical Engineering, Yantai University, Yantai 264005, China.

[e]Institute of Science and Technology for New Energy, Xi'an Technological University, Xi'an, 710021, China.

[†]These authors contributed equally to this work.

*Corresponding author:

Email: mselyf@zju.edu.cn (Y.F.L.); f_fang@fudan.edu.cn (F.F.), jjj_hu@163.com (J.J.H.)

Abstract:

Transition metal catalysts are particularly effective in improving the reaction kinetics of light metal hydrides for reversible hydrogen storage. Herein, tetragonal ZrO_2 hierarchical nanoparticles (nano-ZrO_2) composed of primary particles of ~ 4 nm in diameter are successfully synthesized by a facile one-pot solvothermal process. The unique hierarchical structure features homogeneous distributions of *in situ* formed multivalent Zr-based species, which allow superior catalytic activity for hydrogen storage in MgH_2. The MgH_2+10 wt% nano-ZrO_2 starts releasing H_2 at 163 °C after one activation, which is 107 °C lower than additive-free MgH_2, and 50 °C lower than that of bulk ZrO_2-doped MgH_2. At 230 °C, 5.9 wt% of H is rapidly liberated within 20 min from the nano-ZrO_2-containing MgH_2. More importantly, the material shows superior hydrogenation kinetics compared with all reported catalyst-modified MgH_2. The nano-ZrO_2-

containing Mg took up 4.0 wt% of H in only 12 s at 100 °C under 50 bar H_2, 400 times faster than the bulk-ZrO_2-modified sample. Even at 50 °C, approximately 1.8 wt% H was absorbed within 1 min. Our findings provide useful insights into the design and development of high-performance catalysts towards solid-state hydrogen storage materials.

Keywords: hydrogen storage, magnesium hydride, transition metal, hierarchical nanoparticles, ZrO_2

1. Introduction

It has become imperative to reduce the carbon dioxide emission to address climate change. Hydrogen is regarded as a clean energy carrier due to its high energy density, abundancy, and free of pollution when consumed [1-3]. However, its widespread use as a fuel is still hindered by the lack of a safe, efficient and cost-effective hydrogen storage technique [4,5]. As a typical solid-state hydrogen storage material, magnesium hydride (MgH_2), with high hydrogen capacity (7.6 wt%) and excellent reversibility, has been extensively studied in the past. However, the stable thermodynamics (ΔH: ~76 kJ mol^{-1} of H_2) and high kinetics barriers (ΔE: ~160 kJ mol^{-1}) results in high operating temperatures and sluggish kinetics for storing hydrogen in MgH_2, which largely restricts its practical applications [6]. Over the past five decades, a variety of strategies, including alloying, nanostructuring, catalyzing, and the combinations thereof have been developed to tune the thermodynamics and kinetics of MgH_2 [7-12].

Typically, the hydrogen absorption process by metals or alloys consists of several sequential steps, including (i) the adsorption of molecular hydrogen at the surface, (ii) the dissociation of molecular hydrogen to atomic hydrogen, (iii) the absorption of atomic hydrogen, (iv) the diffusion of absorbed atomic hydrogen and (v) the formation of metal-hydrogen bond. This process has to overcome the dissociation and diffusion energy barriers and may therefore require thermal or catalytic activation, especially for the light metals without d-electron [13].

Catalyst has also been introduced to facilitate dissociation of molecular hydrogen during hydrogenation reaction in metal hydride systems [14]. After decades of research, transition metals and their compounds are demonstrated to be effective in catalyzing hydrogen storage process of MgH_2 [15-24]. In particular, nanostructured transition metal-based catalysts offer effective catalytic activity in the systems [25-34]. Zhang et al. synthesized 10 nm-sized TiO_2@C nanocrystallines by calcinating Ti-MOFs in Ar, which enabled hydrogen release commencing from 205 °C and up to 5.0 wt% H was desorbed within 10 min at 250 °C [26]. The desorption temperature of MgH_2 was successfully decreased to 200 °C by Nb_2O_5 with high surface area [27]. A rapid desorption was observed for MgH_2 doped with TiO_2 nanosheets, which desorbed 5.8 wt% H in 6 min at 240 °C [29]. The Ni-doped ultrafine TiO_2 enabled Mg to pick up 4.5 wt% H even at 50 °C [30]. The rehydrogenation of nano-V_2O_3@C-modified MgH_2 was completed within 700 s at 150 °C under 50 bar H_2 [31]. At 150 °C under 20 bar H_2, a Mg-Ni-VO_x/AC composites absorbed 6.2 wt% H within only 1 min [32]. By adding Nb_2O_5 nanorods supported by graphene, the dehydrogenated MgH_2 sample absorbed 6.0 wt% H at room temperature over 48 hrs [34]. Based upon the literature studies, catalyst can reduce the operating temperatures and improve reaction kinetics, but further enhancements are still needed to make MgH_2 suitable for practical applications.

In this work, we demonstrate hierarchical nanostructured tetragonal ZrO_2 with superior catalytic activity, which enables ultrafast hydrogenation of Mg. As a typical transition metal, Zr sits next to Ti and Nb in the periodic table and is therefore anticipated to be of high catalytic activity. However, few attention has been paid to Zr-based catalysts for hydrogen storage in MgH_2. Herein, through a facile one-pot solvothermal process, we successfully synthesized hierarchical nanostructured tetragonal ZrO_2 powders, which are composed of ~4 nm-sized ultrafine primary nanoparticles. The resultant nano-ZrO_2 largely reduces the onset temperature of dehydrogenation of MgH_2 from 270 to 163 °C, and hydrogen desorption amounts to 5.9 wt% within 20 min at 230 °C. Moreover, an ultrafast hydrogenation is achieved, with 4.0 wt% H

rapidly absorbed by the dehydrogenated nano-ZrO_2-containing MgH_2 within only 12 s at 100 °C under 50 bar H_2, superior to all the known catalyst-modified Mg-based hydrogen storage materials.

2. Experimental section

2.1 Synthesis of nano-ZrO_2

The hierarchical nanostructured ZrO_2 was synthesized by a solvothermal process illustrated in Fig. 1a. Approximate 3.0 g of zirconium isopropoxide isopropanol complex ($C_{15}H_{36}O_5Zr$, Aldrich, 99.9%) was first added into 50 mL of benzyl alcohol (Alfa Aesar, 99%) and stirred for 1 h. The mixture was subsequently added into a 100 mL autoclave, sealed and heated at 210 °C for 48 h with constant stirring. After cooling to ambient temperature, the light yellowish turbid suspension was centrifugated followed by washing with deionized water and ethanol for several times. Finally, the white precipitate was collected and dried at 60 °C overnight to obtain resultant products.

2.2 Preparation of catalyzed MgH_2 system

MgH_2 was synthesized in our own laboratory as reported before [23]. The MgH_2+x wt% nano-ZrO_2 (x = 1, 3, 5, 7, 10) composites were prepared by mechanical milling using a planetary ball mill (QM-3SP4, Nanjing). Nano-ZrO_2 and MgH_2 were weighed and added into a stainless milling jar in an Ar-filled glovebox (Etelux, Lab 2000, China). The ball-to-sample ratio was set at 120:1. To avoid the possible decomposition of MgH_2 caused by temperature increase during the milling process, the milling jar was charged with 10 bar H_2. Ball milling was conducted at 500 rpm for 3 hrs. For comparison, pristine MgH_2 and commercial bulk ZrO_2-doped MgH_2 were also treated under identical conditions. Here, bulk ZrO_2 with 99% purity was purchased from Aladdin.

2.3 Characterization methods

X-ray diffraction (XRD) characterizations were carried out on a Rigaku MiniFlex 600 (Japan)

with Cu K_α radiation operated at 40 kV and 15 mA with a scanning rate of 10° min^{-1}. A custom-designed sample holder covered with Scotch tape was used to prevent exposure of samples to air and moisture during the tests. X-ray photoelectron spectroscopy (XPS) measurements were performed on a Thermo Scientific ESCALAB 250Xi with a monochromatic Al K_α X-ray source (1486.6 eV) under a base pressure of 3.7×10^{-10} Torr. The adventitious C peak at 284.8 eV was used as the reference to calibrate XPS data. Scanning electron microscope (SEM, Hitachi SU8010) and transmission electron microscope (TEM, FEI Tecnai G2 F20 S-TWIN) were employed to observe morphologies and analyze microstructures. Elemental distribution was characterized by energy dispersive X-ray spectrometer (EDS, X-Max) attached to SEM and TEM facilities. The particle size distribution of oleic acid-modified nano-ZrO_2 was estimated by a nanoparticle size analyzer (Zetasizer Nano-ZS, Malvern, UK).

A home-built temperature-programmed desorption (TPD) system equipped with a mass spectrometer (MS, Hiden QIC-20) was used to measure hydrogen desorption. Approximately 15 mg of sample was loaded into a stainless-steel tube reactor and heated from ambient temperature to a desired temperature at a preset heating rate with Ar as a carrier gas. The quantitative measurements of hydrogen desorption and absorption were conducted on a homemade Sievert's type apparatus. For non-isothermal tests, the sample was gradually heated up with a heating rate of 2 °C min^{-1} under vacuum. The dehydrogenated sample was rehydrogenated from room temperature to 250 °C at 1 °C min^{-1} with an initial hydrogen pressure of 50 bar. For isothermal experiments, the sample was first quickly (10 °C min^{-1}) heated to the desired temperature and then maintained for a certain duration at this temperature. Thermal analysis was conducted on a differential scanning calorimetry unit (DSC, NETZSCH 200F3) inside a glovebox. About 3 mg sample was loaded into an alumina crucible and then heated with a heating rate of 2 °C min^{-1} without purge gas.

3. Results and discussion

3.1 Characterization of synthesized nano-ZrO_2

Fig. 1b shows the XRD profile of the prepared nano-ZrO_2. The diffraction pattern matches well with that of tetragonal ZrO_2 (JCPDS: 50-1089), but all the peaks are broad due to the reduced crystallite sizes. With the Scherrer equation, the crystallite sizes were calculated to be approximately 3 nm. The selected area electronic diffraction (SAED) further confirms the presence of polycrystalline tetragonal ZrO_2 (Fig. 1c). SEM observation displays 50-100 nm-sized particles (Fig. 2a) that consist of 3-5 nm primary particles as indicated by TEM (Fig. 2b). High-resolution TEM observation displays lattice fringes with interplanar spacings of 0.295 nm, corresponding to the (011) planes of tetragonal ZrO_2 (Fig. 2c). To verify the primary particle sizes, the solid powders obtained by centrifugation were redispersed in tetrahydrofuran after functionalized with oleic acid for TEM observation [35]. As shown in Fig. 2d, a uniform and highly dispersed nanoparticles with <5 nm in diameter were observed. The average particle size was measured by a laser size analyzer to be ~4 nm (the inset of Fig. 2d). Since the final product was collected through drying the solvothermal solid powders at 60 °C, we believe that the resultant larger ZrO_2 nanoparticles (50-100 nm) are aggregation of 3-5 nm primary nanoparticles, giving rise to a hierarchical nanostructure.

3.2 Catalytic effect of nano-ZrO_2 on MgH_2

The resultant hierarchical nanostructured ZrO_2 was milled with MgH_2 to evaluate its catalytic performance. Six samples with compositions of MgH_2+x wt% nano-ZrO_2 (x = 0, 1, 3, 5, 7 and 10) were prepared. After ball milling treatment, the XRD reflections of MgH_2 still dominate the XRD profiles (Fig. 3a). In addition, two diffraction peaks belonging to MgO are present although their intensities are quite weak. The formation of MgO is likely due to the reaction between MgH_2 and ZrO_2 during ball milling (see XPS sections). The diffraction peaks become broader with increasing loading of nano-ZrO_2, indicating that crystallites became smaller or amorphized due to the higher milling efficiency caused by the high hardness of ZrO_2 (~13 GPa) [36], which therefore functions as a grinding aid.

The milled composites were subjected to hydrogen desorption and absorption tests under identical conditions. In the TPD curves (Fig. 3b), a dramatic low-temperature shift is observed in hydrogen desorption for the nano-ZrO_2-containing samples. With respect to pristine MgH_2, the addition of 1 wt% nano-ZrO_2 reduces the desorption peak temperature from 327 to 262 °C, which was further decreased to 235 °C for the 7 wt% nano-ZrO_2-containing sample, representing a reduction of 92 °C. No additional reduction in the peak temperature was observed when further increasing loading of nano-ZrO_2 to 10 wt%. This improved desorption performance was confirmed with the quantitative volumetric release measurements. As shown in Fig. 3c, most of the hydrogen desorption from pristine MgH_2 took place at 300-380 °C with an onset temperature of around 270 °C. The total amount of desorption was determined to be 7.4 wt%, very close to 7.6 wt% of the theoretical value. The addition of nano-ZrO_2 induces a gradual decrease in the desorption temperature along with a slight reduction in capacity. For the MgH_2+1 wt% nano-ZrO_2 sample, the hydrogen desorption started from 220 °C and completed at 330 °C with a capacity of 7.2 wt%. Here, about 7 wt% of hydrogen was liberated below 290 °C. Increasing the nano-ZrO_2 loading to 7 wt%, the onset temperature of desorption dropped to 190 °C and the available hydrogen capacity was measured to be 6.7 wt%. When the content of nano-ZrO_2 was further increased to 10 wt%, the desorption temperature remained nearly unchanged but the capacity reduced to 6.5 wt%. The drop in capacity is likely due to the reaction between MgH_2 and ZrO_2, as discussed in later section.

The hydrogenation test was carried out under 50 bar H_2. Fig. 3d presents the amount of hydrogen uptake as a function of temperature. The rehydrogenation performance was significantly improved with the presence of nano-ZrO_2, especially for the samples with higher nano-ZrO_2 loading, and the MgH_2+10 wt% nano-ZrO_2 sample absorbed ~6.4 wt% H below 200 °C. The hydrogen uptake was clearly detected even at 25 °C for the samples with ≥ 5 wt% nano-ZrO_2, which is 81 °C lower than that of the dehydrogenated pristine sample (106 °C). Re-dehydrogenation took place at lower temperatures. As shown in Fig. S1, the onset temperature

of the 2nd desorption of 10 wt% nano-ZrO_2-containing sample was further reduced by 23 °C, to 163 °C, compared to the as-milled sample. This indicates a continuous formation of catalytic species during initial hydrogen cycling, as seen from XPS results below.

The catalytic activity of hierarchical nanostructured ZrO_2 is much better than commercial bulk ZrO_2 (200-300 nm, polyhedral morphology, Fig. S2), as shown in Fig. 4a and b. There exists a strong dependence of (de)hydrogenation temperatures on the milling durations for the bulk ZrO_2-containing sample (Fig. 4c and d). In contrast, the desorption and absorption curves are very similar for nano-ZrO_2 containing samples ball milled for 3 and 12 hrs (Fig. 4e and f). This is likely related to the unique hierarchical nanostructure of prepared ZrO_2, which allows homogeneous and highly dispersed distribution of active catalytic species in a short milling treatment. Such speculation is verified by EDS mapping examination (Fig. 5). For MgH_2+10 wt% nano-ZrO_2 sample, elemental Zr distributes homogeneously in the system after 3 hrs of ball milling (Fig. 5a). In contrast, severe aggregation was observed for bulk ZrO_2-containing sample (Fig. 5b). The inhomogeneous distribution of Zr was still visible even after 12 hrs ball milling albeit weakened to some extent (Fig. 5c). We also noticed that the catalytic activity of nano-ZrO_2 slightly decreased after being calcined at 400 °C for 12 h, which is due to the sintering-led particle agglomeration that induces the inhomogeneous distribution (Fig. S3).

Isothermal measurements also display remarkable improvement in (de)hydrogenation by nano-ZrO_2 (Fig. 6 and Fig. S4). Bulk ZrO_2-containing MgH_2 desorbed ~5.3 wt% H within 60 mins at 230 °C (Fig. 6a). In contrast, it took only 4 mins to release the identical H quantity for the nano-ZrO_2-containing sample. The average desorption rate was increased by 15 times (Fig. 6b). At 185 °C, the MgH_2+10 wt% nano-ZrO_2 sample liberated 1.5 wt% H within 10 mins, while no hydrogen release was detected for the bulk-ZrO_2-modified sample under identical conditions (Fig. S4). More encouragingly, the presence of nano-ZrO_2 enables an ultrafast hydrogen absorption. As illustrated in Fig. 6c and Table 1, the dehydrogenated nano-ZrO_2-containing sample rapidly took up 5.9 wt% H within 6 s at 200 °C, whereas the bulk-ZrO_2-

containing sample needed 20 mins to absorb only ~4.9 wt% H at 200 °C (Fig. S5). When operated at 150 and 100 °C, hydrogen uptake by the nano-ZrO_2-containing sample reached 5.2 wt% within 6 s and 4.0 wt% H within 12 s, respectively. Even at 50 °C, the capacity reached 1.8 wt% H within 1 min. For the bulk-ZrO_2-containing sample, they were 3.1 wt% (150 °C), 1.0 wt% H (100 °C) and 0.45 wt% H (50 °C) within 20 mins, respectively (Fig. S5). The average absorption rate at 100 °C was found to be enhanced by approximately 400 times (Fig. 6d). Such superior hydrogen sorption outperforms all known catalyst-modified MgH_2 hydrogen storage systems (Fig. 6e) [16-19,26,28,30,31,33,37-45].

The cycling performances were further measured by isothermal desorption and absorption. In contrast to the bulk-ZrO_2-containing MgH_2, where the desorption capacity decreased from 6.5 to 5.9 wt% after two cycles (Fig. 7a), no appreciable capacity degradation was detected for the nano-ZrO_2-containing sample after 10 cycles (Fig. 7b). In contrast to the bulk-ZrO_2-modified MgH_2 (Fig. 7c), nano-ZrO_2-containing sample displayed similar performance with no capacity decay in the isothermal desorption (Fig. 7d). All these results demonstrate a durable and superior catalytic activity for the hierarchical nanostructured ZrO_2.

3.3 Desorption enthalpy change and energy barrier

To understand the role played by nano-ZrO_2, the desorption enthalpy change and kinetic energy barrier were determined by DSC and Kissinger's methods, respectively. The results are shown in Fig. 8. In comparison with pristine MgH_2, a remarkable low-temperature shift of the desorption peak was observed in the DSC curve of MgH_2+10 wt% nano-ZrO_2 sample (Fig. 8a), in good agreement with TPD measurement. By integrating the endothermic peak area, the desorption enthalpy change was determined to be 74.1 kJ mol^{-1} of H_2 for the nano-ZrO_2-containing sample, very similar to the value of pristine MgH_2 (~76 kJ mol^{-1} of H_2), indicating that the presence of nano-ZrO_2 did not change the dehydrogenation thermodynamics of MgH_2. As demonstrated by Kissinger's plot (Fig. 8b), the apparent activation energy of MgH_2+10 wt% nano-ZrO_2 sample was approximately 86.4 kJ mol^{-1}, which is ~61% that of the pristine MgH_2

(140.5 kJ mol^{-1}). This value is also ~12.5 kJ mol^{-1} lower than that of 10 wt% bulk-ZrO_2-containing sample (98.9 kJ mol^{-1}) (Fig. S6), further confirming the catalytic effect of hierarchical nano-ZrO_2. As such, we attribute the remarkably decreased desorption temperature mainly to the low kinetic energy barrier in the nano-ZrO_2 sample.

The rate-controlling steps were elucidated by analyzing the isothermal desorption data (Fig. 8c,d). Hydrogen desorption from the bulk-ZrO_2-containing MgH_2 agrees with the nucleation and growth model (A2 model), identical to pristine MgH_2 reported previously [17], while the nano-ZrO_2-modified MgH_2 fits better with the three-dimensional phase boundary model (R3 model). Thus, quite different from pristine and bulk-ZrO_2-containing MgH_2, the hydrogen desorption process of nano-ZrO_2 doped MgH_2 was limited by phase boundary expansion rather than the nucleation of metallic Mg. This is possibly due to the fact that the hierarchical nanostructure enables homogeneous and highly dispersed Zr active catalytic species as evidenced by EDS mapping analyses (Fig. 5a), which facilitates not only the dissociation of Mg-H/H-H bonding but also nucleation by functioning as nucleation sites, consequently reducing the kinetic energy barrier. This significantly improved hydrogen storage kinetics of nano-ZrO_2-containing MgH_2, including reduced desorption/absorption temperatures and enhanced desorption/absorption rates. As for the bulk-ZrO_2-containing sample, the inhomogeneous distribution of Zr makes the nucleation sites insufficient, accordingly contributing the limited catalytic activity.

3.4 The active catalytic species

As mentioned above, lower desorption temperatures were attained after one-cycle desorption and absorption. This is likely related to the evolving chemical states of Zr-based active catalytic species, which was studied by high-resolution XPS analyses (Fig. 9). Note that Zr-based species were not detected by means of XRD likely due to low concentration (Fig. 3a). As shown in Fig. 9a, the high-resolution Zr XPS spectrum of the milled nano-ZrO_2-containing sample can be deconvoluted into four peaks at 184.2, 182.0, 181.8 and 179.6 eV. Two peaks at 184.2 and

181.8 eV can be assigned to the Zr $3d_{3/2}$-$3d_{5/2}$ spin-orbit doublet of ZrO_2, and the other two peaks at 182.0 and 179.6 eV agree well with the binding energies reported for $ZrH_{1.64}$ [46], which was *in situ* formed due to the reaction between ZrO_2 and MgH_2 during ball milling. After the first dehydrogenation, two characteristic peaks of ZrO_2 are still visible, but the two peaks associated with $ZrH_{1.64}$ disappeared with the appearance of two new peaks at 180.7 and 178.3 eV which are from metallic Zr along (Fig. 9b). A portion of metallic Zr was converted into $ZrH_{1.64}$ again in the follow-up hydrogenation process (Fig. 9c), and the regeneration of metallic Zr occurred after the second dehydrogenation (Fig. 9d). Activation, i.e. one cycle desorption and adsorption, gives rise to a typical multi-valent Zr chemical environment, especially in the recharged samples where Zr^{4+}, $Zr^{1.64+}$ and Zr^0 all exist. These Zr species facilitate the H-H and Mg-H dissociation in the MgH_2/Mg matrix, as the case in multi-valent Ti-modified MgH_2 system [24]. In contrast, only two characteristic XPS peaks of Zr^{4+} in ZrO_2 were identified in the bulk-ZrO_2-containing MgH_2, after milling, dehydrogenation and even hydrogenation (Fig. S7), indicating that no reduction reaction occurred for bulk ZrO_2, possibly due to the low reactivity caused by the large particle size. This is responsible for its relatively poor catalytic effectiveness.

TEM, HRTEM and EDS studies of the post-cycled MgH_2+10 wt% nano-ZrO_2 sample were carried out to understand the stability of Zr-based catalysts. As shown in Fig. S8, Zr and O are still homogeneously dispersed in MgH_2 matrix after 10 cycles. The particle size of Zr-based species stabilized at ~4 nm as well. The preservation of good dispersity and small size is important for the superior cyclability of nano-ZrO_2-containing MgH_2.

4. Conclusion

In this work, a unique hierarchical nanostructured ZrO_2 composed of ~4 nm-sized ultrafine primary nanoparticles was successfully synthesized through a simple one-pot solvothermal process. The resultant nano-ZrO_2 exhibited superior catalytic activity for the hydrogen cycling

by MgH_2, as evidenced by significantly reduced operation temperatures and ultrafast hydrogenation kinetics. The addition of 10 wt% nano-ZrO_2 reduced the onset dehydrogenation temperature of MgH_2 from 270 to 163 °C, and enabled a rapid release of 5.3 wt% H within 4 mins at 230 °C. In addition, the dehydrogenated sample rapidly absorbed 4.0 wt% H within only 12 s at 100 °C under 50 bar H_2, which represents the fastest hydrogenation for catalyst-modified Mg-based hydrogen storage materials under identical conditions. The nano-ZrO_2-doped MgH_2 displayed good stability over 10 cycles of hydrogen desorption and absorption. The superior catalytic activity of nano-ZrO_2 can be attributed to the multivalent Zr-based active species homogeneously distributed in the hierarchical nanostructures. This finding brings MgH_2 a step forward for practical applications and provides a rational design of catalysts for light-metal hydride based hydrogen storage materials.

Notes

The authors declare no competing financial interest.

Data availability

All data included in this study are available upon request from the corresponding author.

Acknowledgements

We gratefully acknowledge the financial support received from the National Key R&D Program of China (2018YFB1502102), the Natural Science Foundation of Zhejiang Province (LD21E010002), the National Outstanding Youth Foundation of China (52125104), the National Natural Science Foundation of China (52001277), the Fundamental Research Funds for the Central Universities (2021FZZX001-09), and the National Youth Top-Notch Talent Support Program.

Appendix A. Supplementary data

Supplementary data associated with this article can be found in the online version at doi:

References

[1] L. Schlaphach, A. Züttel, Hydrogen-storage materials for mobile applications, Nature 414 (2001) 353–358.

[2] I.P. Jain, Hydrogen the fuel for 21st century, Int. J. Hydrogen Energy 34 (2009) 7368–7378.

[3] T. He, P. Pachfule, H. Wu, Q. Xu, P. Chen, Hydrogen carriers, Nat. Rev. Mater. 1 (2016) 16067.

[4] E. Abohamzeha, F. Salehi, M. Sheikholeslami, R. Abbassi, F. Khan, Review of hydrogen safety during storage, transmission, and applications processes, J. Loss Prevent Proc. 72 (2021) 104569.

[5] A, Schneemann, J.L. White, S.Y. Kang, S. Jeong, L.F. Wang, E.S. Cho, T.W. Heo, D. Prendergast, J.J. Urban, B.C. Wood, M.D. Allendorf, V. Stavila, Nanostructured Metal Hydrides for Hydrogen Storage, Chem. Rev. 118 (2018) 10775–10839.

[6] V.A. Yartys, M.V. Lototskyy, E. Akiba, R. Albert, V.E. Antonov, J.R. Ares, M. Baricco, N. Bourgeois, C.E. Buckley, J.M. Bellosta von Colbe, J.-C. Crivello, F. Cuevas, R.V. Denys, M. Dornheim, M. Felderhoff, D.M. Grant, B.C. Hauback, T.D. Humphries, I. Jacob, T.R. Jensen, P.E. de Jongh, J.-M. Joubert, M.A. Kuzovnikov, M. Latroche, M. Paskevicius, L. Pasquini, L. Popilevsky, V.M. Skripnyuk, E. Rabkin, M.V. Sofianos, A. Stuart, G. Walker, H. Wang, C.J. Webb, M. Zhu, Magnesium based materials for hydrogen based energy storage: Past, present and future, Int. J. Hydrogen Energy 44 (2019) 7809–7859.

[7] X.L. Zhang, Y.F. Liu, X. Zhang, J.J. Hu, M.X. Gao, H.G. Pan, Empowering hydrogen storage performance of MgH_2 by nanoengineering and nanocatalysis, Mater. Today Nano 9 (2020) 100064.

[8] J.G. Zhang, Y.F. Zhu, L.L. Yao, C. Xu, Y.N. Liu, L.Q. Li, State of the art multi-strategy improvement of Mg-based hydrides for hydrogen storage, J. Alloys Compd. 782 (2019) 796–823.

[9] J.F. Zhang, Z.N. Li, Y.F. Wu, X.M. Guo, J.H. Ye, B.L. Yuan, S.M. Wang, L.J. Jiang, Recent advances on the thermal destabilization of Mg-based hydrogen storage materials, RSC Adv. 9 (2019) 408–428.

[10] X.B. Xie, M. Chen, M.M. Hu, B.L. Wang, R.H. Yu, T. Liu, Recent advances in magnesium-based hydrogen storage materials with multiple catalysts, Int. J. Hydrogen Energy 44 (2019) 10694–10712.

[11] J. Zhang, S. Yan, H. Qu, Recent progress in magnesium hydride modified through catalysis and nanoconfinement, Int. J. Hydrogen Energy 43 (2018) 1545–1565.

[12] Y.H. Sun, C.Q. Shen, Q.W. Lai, W. Liu, D.W. Wang, K.F. Aguey-Zinsou, Tailoring magnesium based materials for hydrogen storage through synthesis: Current state of the art, Energy Storage Mater. 10 (2018) 168–198.

[13] V. Bérubé, G. Radtke, M. Dresselhaus, G. Chen, Size effects on the hydrogen storage properties of nanostructured metal hydrides: A review, Int. J. Energy Res. 31 (2007) 637–663.

[14] B. Sakintuna, F. Lamari-Darkrim, M. Hirscher, Metal hydride materials for solid hydrogen storage: A review, Int. J. Hydrogen Energy 32 (2007) 1121–1140.

[15] R.L. Holtz, M.A. Imam, Hydrogen storage characteristics of ball-milled magnesium-nickel and magnesium-iron alloys, J. Mater. Sci. 34 (1999) 2655–2663.

[16] L.T. Zhang, L. Ji, Z.D. Yao, N.H. Yan, Z. Sun, X.L. Yang, X.Q. Zhu, S.L. Hu, L.X. Chen, Facile synthesized Fe nanosheets as superior active catalyst for hydrogen storage in MgH_2, Int. J. Hydrogen Energy 44 (2019) 21955–21964.

[17] X. Lu, L.T. Zhang, H.J. Yu, Z.Y. Lu, J.H. He, J.G. Zheng, F.Y. Wu, L.X. Chen, Achieving superior hydrogen storage properties of MgH_2 by the effect of TiFe and carbon nanotubes, Chem. Eng. J. 422 (2021) 130101.

[18] Y.F. Liu, H.F. Du, X. Zhang, Y.X. Yang, M.X. Gao, H.G. Pan, Superior catalytic activity derived from a two-dimensional Ti_3C_2 precursor towards the hydrogen storage reaction of magnesium hydride, Chem. Commun. 52 (2016) 705–708.

[19] L.T. Zhang, Z. Sun, Z.D. Yao, L. Yang, N.H. Yan, X. Lu, B.B. Xiao, X.Q. Zhu, L.X. Chen, Excellent catalysis of Mn_3O_4 nanoparticles on the hydrogen storage properties of MgH_2: an experimental and theoretical study, Nanoscale Adv. 2 (2020) 1666–1675.

[20] K. Wang, X. Zhang, Z.H. Ren, X.L. Zhang, J.J. Hu, M.X. Gao, H.G. Pan, Y.F. Liu, Nitrogen-stimulated superior catalytic activity of niobium oxide for fast full hydrogenation of magnesium at ambient temperature, Energy Storage Mater. 23 (2019) 79–87.

[21] M. Ismail, Effect of adding different percentages of $HfCl_4$ on the hydrogen storage properties of MgH_2, Int. J. Hydrogen Energy, 46 (2021) 8621–8628.

[22] H.Z. Liu, C.L. Lu, X.C. Wang, L. Xu, X.T. Huang, X.H. Wang, H. Ning, Z.Q. Lan, J. Guo, Combinations of V_2C and Ti_3C_2 MXenes for Boosting the Hydrogen Storage Performances of MgH_2, ACS Appl. Mater. Interfaces 13 (2021) 13235−13247.

[23] H. Wang, J. Hu, F.G. Han, Y.S. Lu, J.W. Liu, L.Z. Ouyang, M. Zhu, Enhanced joint catalysis of YH_2/Y_2O_3 on dehydrogenation of MgH_2, J. Alloys Compd. 645 (2015) S209–S212.

[24] J. Cui, H. Wang, J.W. Liu, L.Z. Ouyang, Q.G. Zhang, D.L. Sun, X.D. Yao, M. Zhu, Remarkable enhancement in dehydrogenation of MgH_2 by a nano-coating of multi-valence Ti-based catalysts, J. Mater. Chem. A 1 (2013) 5603–5611.

[25] R.A. Varin, T. Czujko, E.B. Wasmund, Z.S. Wronski, Catalytic effects of various forms of nickel on the synthesis rate and hydrogen desorption properties of nanocrystalline

magnesium hydride (MgH_2) synthesized by controlled reactive mechanical milling (CRMM), J. Alloys Compd. 432 (2007) 217–231.

[26] X. Zhang, Z.H. Leng, M.X. Gao, J.J. Hu, F. Du, J.H. Yao, H.G. Pan, Y.F. Liu, Enhanced hydrogen storage properties of MgH_2 catalyzed with carbon-supported nanocrystalline TiO_2, J. Power Sources 398 (2018) 183–192.

[27] V.V. Bhat, A. Rougier, L. Aymard, G.A. Nazri, J.-M. Tarascon, High surface area niobium oxides as catalysts for improved hydrogen sorption properties of ball milled MgH_2, J. Alloys Compd. 460 (2008) 507–512.

[28] M. Zhang, X.Z. Xiao, J.F. Mao, Z.Y. Lan, X. Huang, Y.H. Lu, B.S. Luo, M.J. Liu, M. Chen, L.X. Chen, Synergistic catalysis in monodispersed transition metal oxide nanoparticles anchored on amorphous carbon for excellent low-temperature dehydrogenation of magnesium hydride, Mater. Today Energy 12 (2019) 146–154.

[29] M. Zhang, X.Z. Xiao, X.W. Wang, M. Chen., Y.H. Lu, M.J. Liu, L.X. Chen, Excellent catalysis of TiO_2 nanosheets with high-surface-energy {001} facets on the hydrogen storage properties of MgH_2, Nanoscale 11 (2019) 7465–7473.

[30] J.G. Zhang, R. Shi, Y.F. Zhu, Y.N. Liu, Y. Zhang, S.S. Li, L.Q. Li, Remarkable synergistic catalysis of Ni-doped ultrafine TiO_2 on hydrogen sorption kinetics of MgH_2, ACS Appl. Mater. Interfaces 10 (2018) 24975–24980.

[31] Z.Y. Wang, Z.H. Ren, N. Jian, M.X. Gao, J.J. Hu, F. Du, H.G. Pan, Y.F. Liu, Vanadium oxide nanoparticles supported on cubic carbon nanoboxes as highly active catalyst precursors for hydrogen storage in MgH_2, J. Mater. Chem. A 6 (2018) 16177–16185.

[32] Y. Jia, L.N. Cheng, N. Pan, J. Zou, G.Q. Lu, X.D. Yao, Catalytic De/Hydrogenation in Mg by Co-Doped Ni and VO_x on Active Carbon: Extremely Fast Kinetics at Low Temperatures and High Hydrogen Capacity, Adv. Energy Mater. 1 (2011) 387–393.

[33] J.H. Zang, S.F. Wang, F. Wang, Z.Y. Long, F.J. Mo, Y.H. Xia, F. Fang, Y. Song, D.L. Sun, Li-triggered superior catalytic activity of V in Li_3VO_4: enabling fast and full hydrogenation of Mg at lower temperatures, J. Mater. Chem. A 8 (2020) 14935–14943.

[34] K. Wang, X. Zhang, Y.F. Liu, Z.H. Ren, X.L. Zhang, J.J. Hu, M.X. Gao, H.G. Pan, Graphene-induced growth of N-doped niobium pentaoxide nanorods with high catalytic activity for hydrogen storage in MgH_2, Chem. Eng. J. 46 (2021) 12683.

[35] J. Joo, T. Yu, Y. W. Kim, H. M. Park, F. Wu, J. Z. Zhang, T. Hyeon, Multigram scale synthesis and characterization of monodisperse tetragonal zirconia nanocrystals, J. Am. Chem. Soc. 125 (2003) 6553.

[36] A. Krell, Load dependence of hardness in sintered submicrometer Al_2O_3 and ZrO_2, J. Am. Ceram. Soc. 78 (1995) 1417–1419.

[37] M. Chen, Y.Q. Yi, X.Z. Xiao, Y.H. Lu, M. Zhang, J.G. Zheng, L.X. Chen, Highly efficient ZrH_2 nanocatalyst for the superior hydrogenation kinetics of magnesium hydride under moderate conditions: Investigation and mechanistic insights, Appl. Surf. Sci. 541 (2021) 148375.

[38] X.L. Zhang, K. Wang, X. Zhang, J.J. Hu, M.X. Gao, H.G. Pan, Y.F. Liu, Synthesis process and catalytic activity of Nb_2O_5 hollow spheres for reversible hydrogen storage of MgH_2, Int J Energy Res. 45 (2020) 3129–3141.

[39] M. Zhang, X.Z. Xiao, Z.M. Hang, M. Chen, X.C. Wang, N. Zhang, L.X. Chen, Superior catalysis of NbN nanoparticles with intrinsic multiple valence on reversible hydrogen storage properties of magnesium hydride, Int. J. Hydrogen Energy 46 (2021) 814–822.

[40] S.K. Pandey, A. Bhatnagar, V. Shukla, R. Kesarwani, U. Deshpandey, T.P. Yadav, Catalytic mechanism of TiO_2 quantum dots on the de/re-hydrogenation characteristics of magnesium hydride, Int. J. Hydrogen Energy 46 (2021) 37340–37350.

[41] M. Chen, X.Z. Xiao, M. Zhang, J.F. Mao, J.G. Zheng, M.J. Liu, X.C. Wang, L.X. Chen, Insights into 2D graphene-like TiO_2 (B) nanosheets as highly efficient catalyst for

improved low-temperature hydrogen storage properties of MgH_2, Mater. Today Energy 16 (2020) 100411.

[42] W. Zhu, S. Panda, C. Lu, Z.W. Ma, D. Khan, J.J. Dong, F.Z. Sun, H. Xu, Q.Y. Zhang, J.X. Zou, Using a Self-Assembled Two-Dimensional MXene-Based Catalyst (2D-Ni@Ti_3C_2) to Enhance Hydrogen Storage Properties of MgH_2, ACS Appl. Mater. Inter. 12 (2020) 50333–50343.

[43] L.C. Zhang, K. Wang, Y.F. Liu, X. Zhang, J.J. Hu, M.X. Gao, H.G. Pan, Highly active multivalent multielement catalysts derived from hierarchical porous $TiNb_2O_7$ nanospheres for the reversible hydrogen storage of MgH_2, Nano Res. 14 (2021) 148–156.

[44] M.S. El-Eskandarany, N. Ali, F. Al-Ajmi, M. Banyan, Effect of ZrC Nanopowders on Enhancing the Hydro/Dehydrogenation Kinetics of MgH_2 Powders, Molecules 26 (2021) 4962.

[45] Y.S. Liu, S. Wang, Z.L. Li, M.X. Gao, Y.F. Liu, W.P. Sun, H.G. Pan, Enhanced Hydrogen Storage Performance of MgH_2 by the Catalysis of a Novel Intersected Y_2O_3/NiO Hybrid, Processes 9 (2021) 892.

[46] T.A. Sasaki, Y. Baba, Chemical-state studies of Zr and Nb surfaces exposed to hydrogen ions, Phys. Rev. B 31 (1985) 791–797.

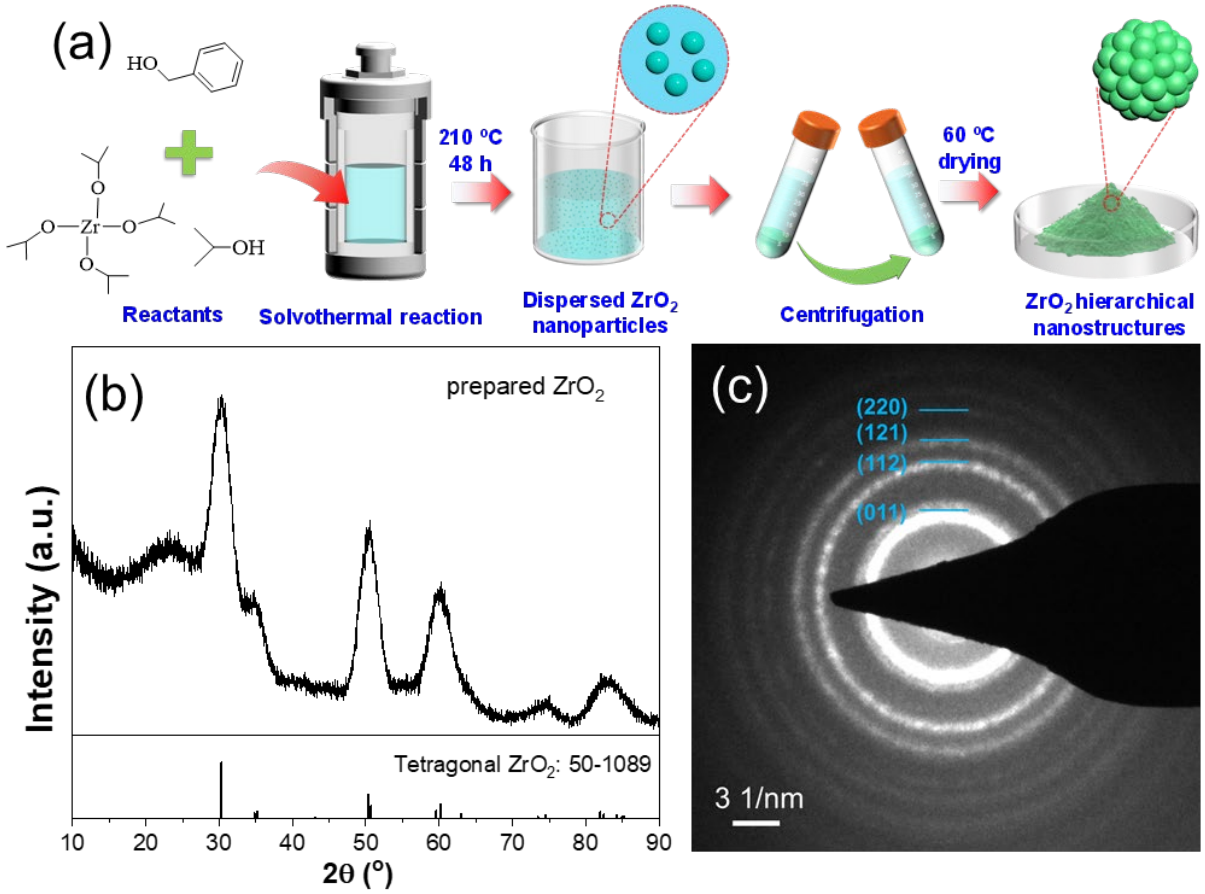

Fig. 1. Synthesis and characterization of tetragonal ZrO_2 hierarchical nanoparticles. (a) Schematic illustration of the preparation process. (b) XRD and (c) SAED patterns of resultant product.

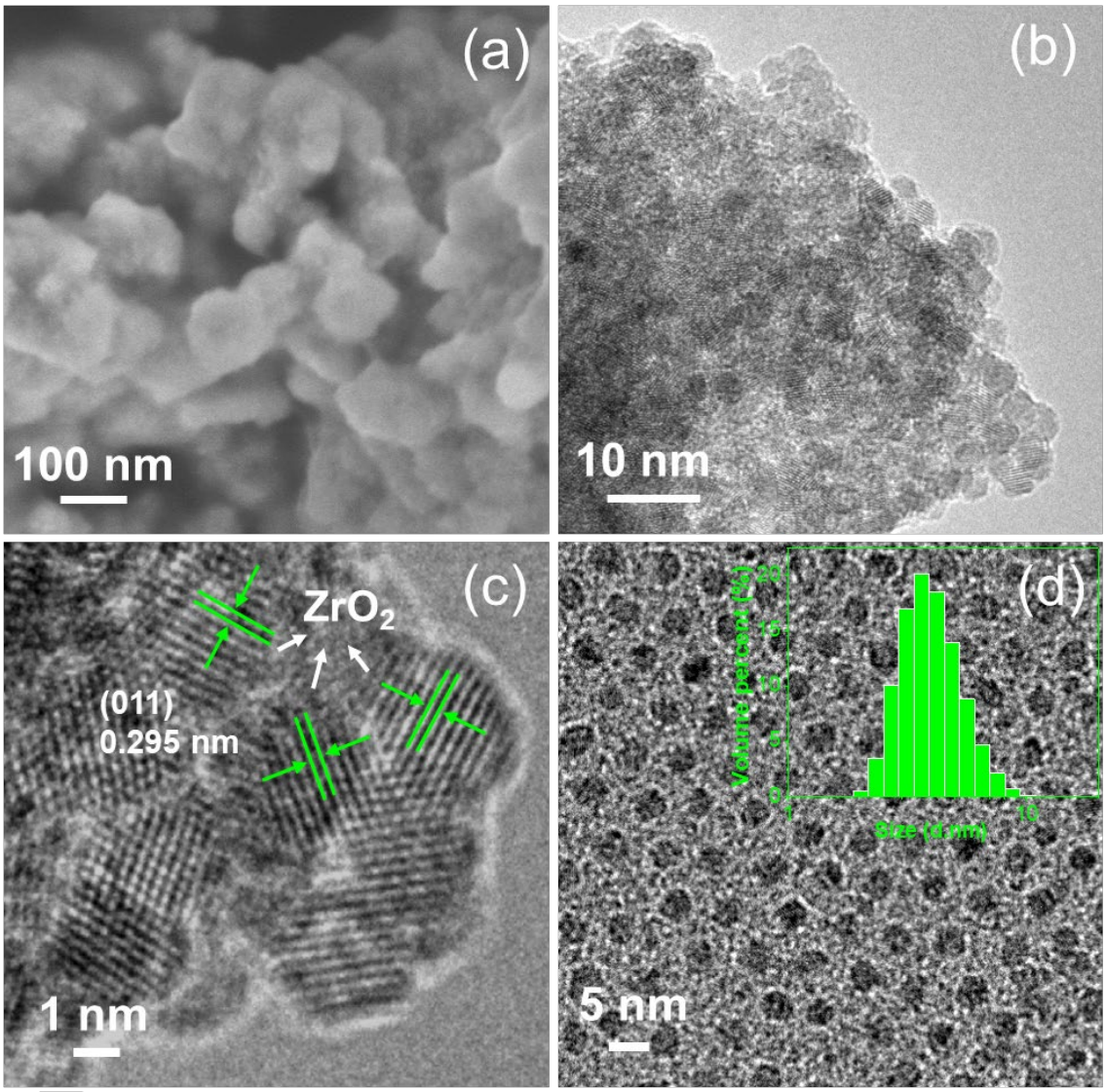

Fig. 2. SEM and TEM observations of tetragonal ZrO_2 hierarchical nanoparticles. (a) SEM, (b) TEM and (c) HRTEM images. (d) TEM image of dispersed ZrO_2 hierarchical nanoparticles. The inset shown in (d) is the particle size distribution measured using a laser size analyzer ($d_{average}$= 4.1 nm).

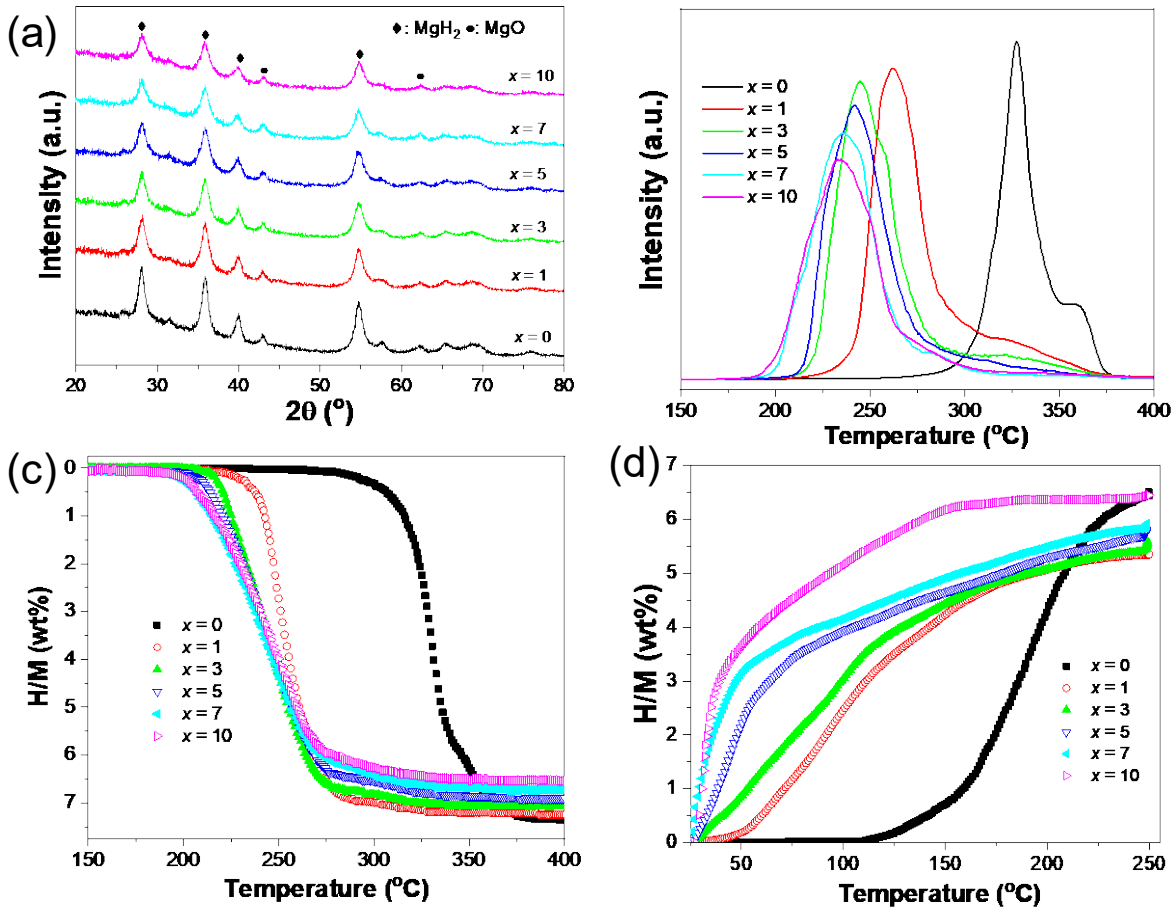

Fig. 3. Structure and performance of MgH_2+*x* wt% nano-ZrO_2 (*x*=0, 1, 3, 5, 7, 10) samples. (a) XRD patterns, (b) TPD, (c) volumetric hydrogen release and (d) non-isothermal hydrogen absorption curves under 50 bar H_2.

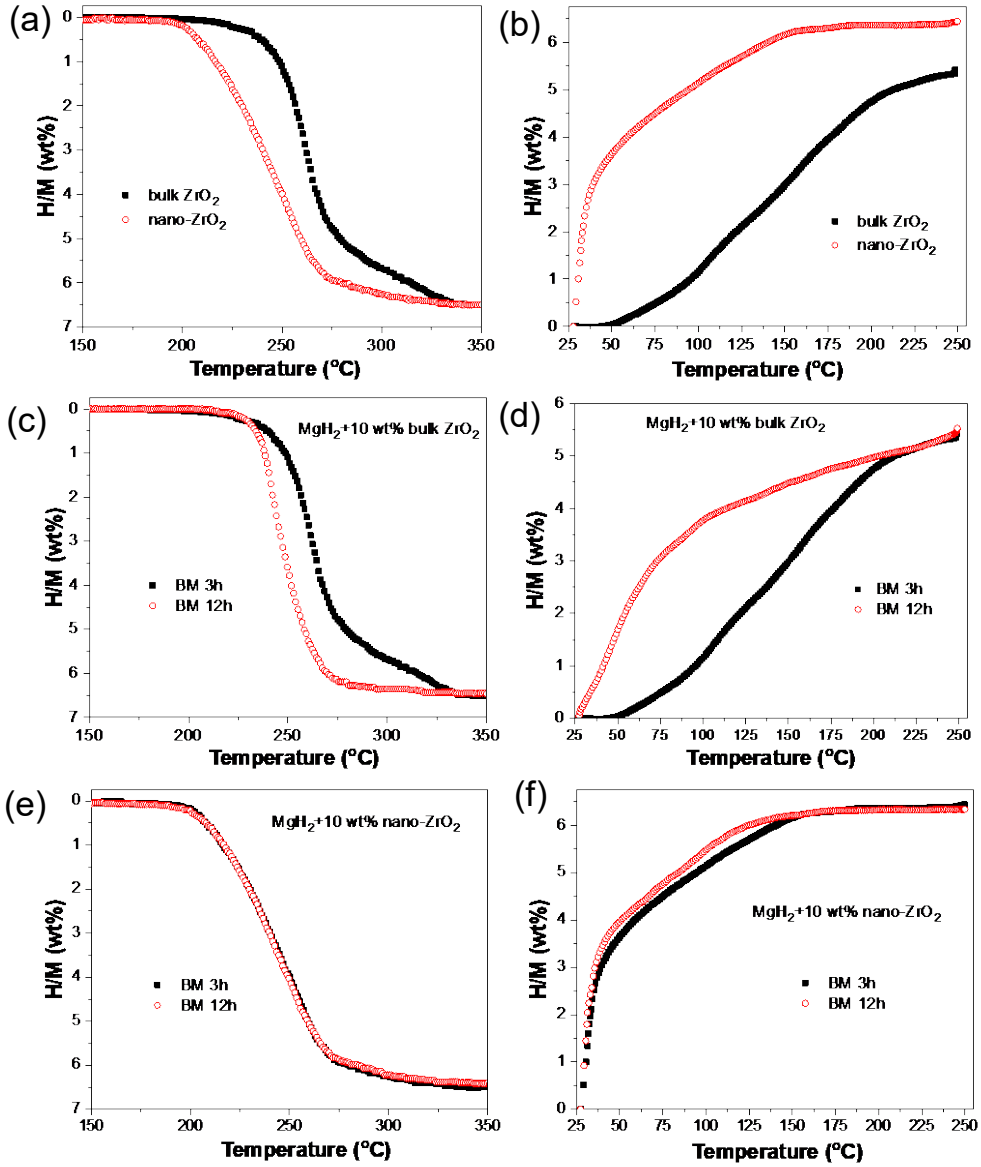

Fig. 4. Hydrogen desorption and absorption of bulk-ZrO_2 and nano-ZrO_2-modified MgH_2. (a, c, e) Volumetric hydrogen release and (b, d, f) non-isothermal absorption curves under 50 bar H_2.

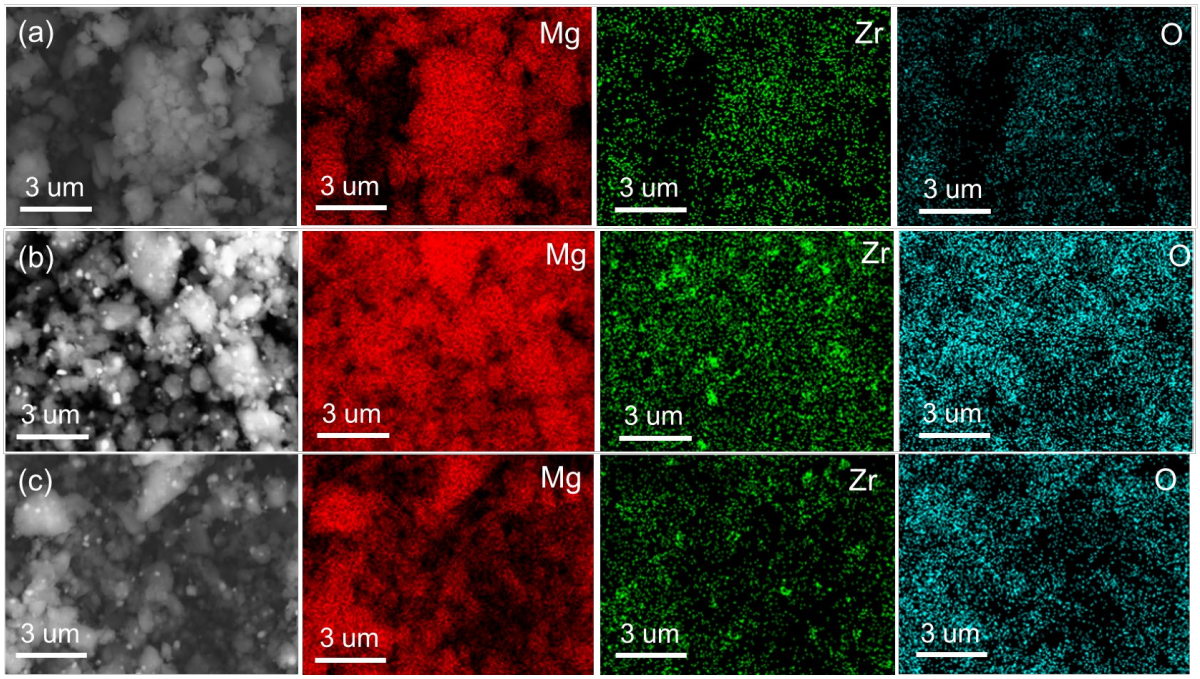

Fig. 5. EDS mapping of Mg, Zr, and O for MgH_2 milled with (a) 10 wt% nano-ZrO_2 for 3 hrs, with 10 wt% bulk ZrO_2 for 3 hrs (b) and 12 hrs (c).

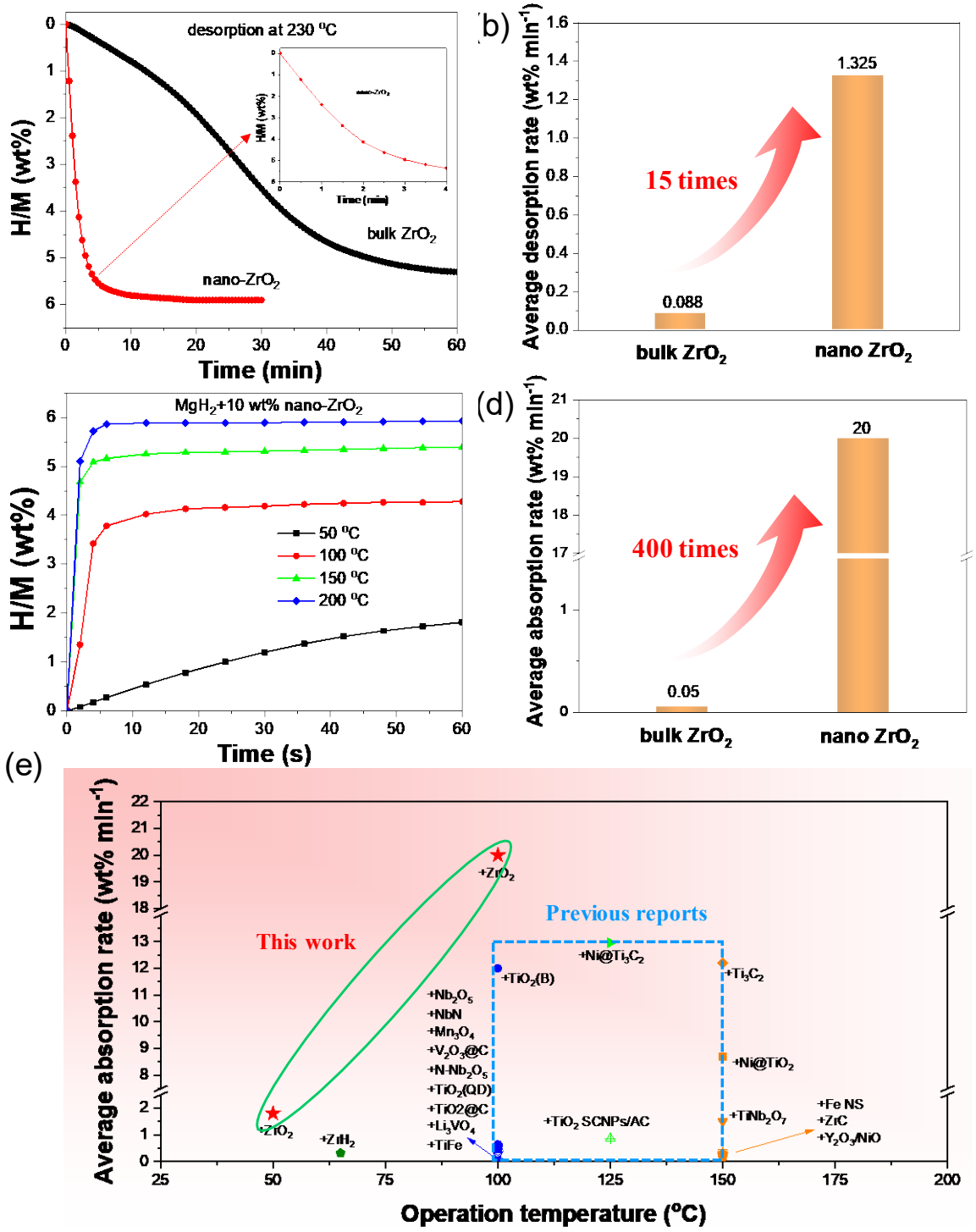

Fig. 6. (a) Isothermal desorption curves and (b) average desorption rates of bulk ZrO_2 and nano-ZrO_2-containig MgH_2 at 230 °C. (c) Isothermal absorption curves of nano-ZrO_2-containing MgH_2 at various temperatures. (d) Average hydrogen absorption rate of dehydrogenated bulk ZrO_2 and nano-ZrO_2-containing MgH_2 at 100 °C under 50 bar H_2. (e) Comparison of average absorption rate of dehydrogenated nano-ZrO_2-containing MgH_2 with reported catalyst-modified samples.

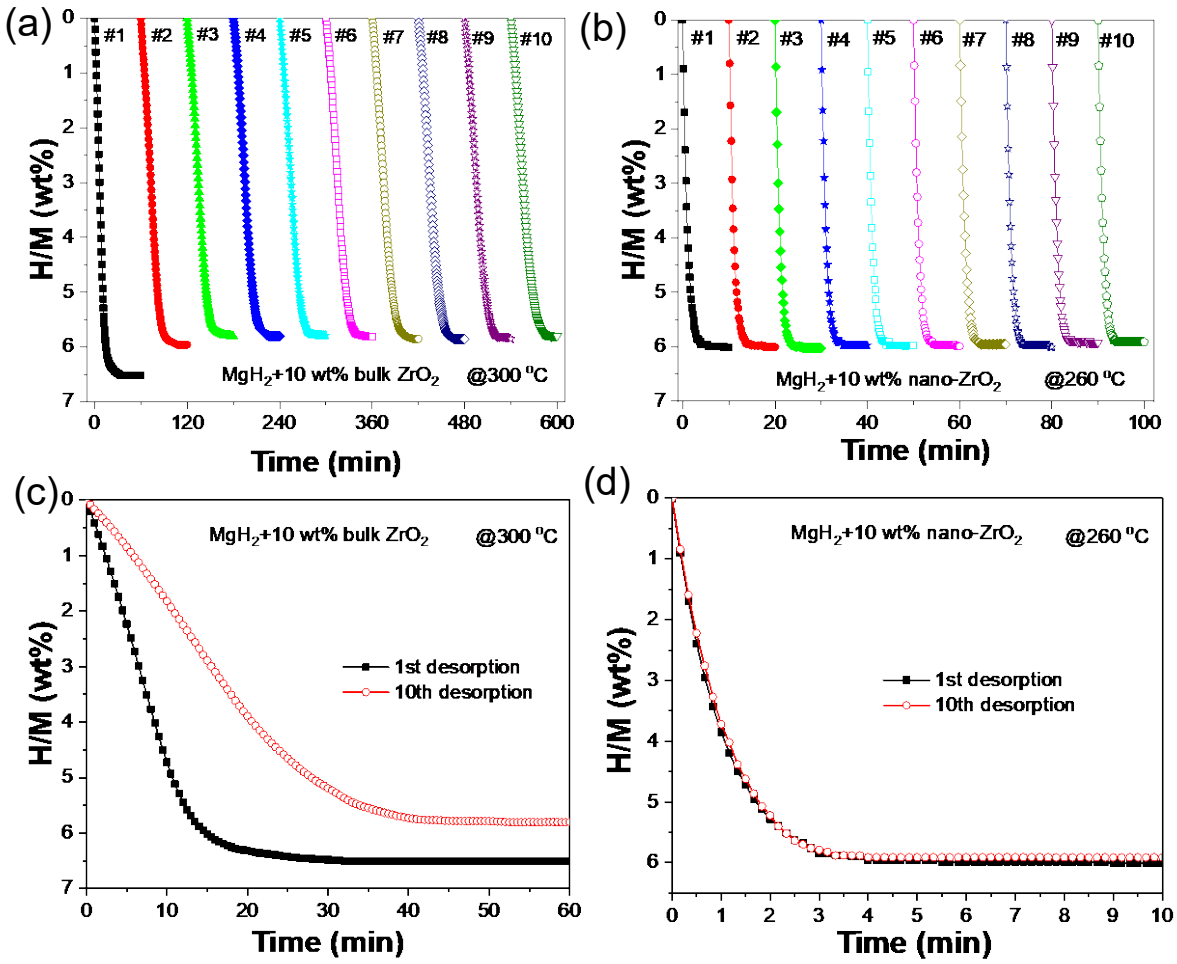

Fig. 7. Cycling stability of (a) bulk ZrO_2 and (b) nano-ZrO_2-containing MgH_2. Hydrogen desorption curves of (c) bulk ZrO_2 and (d) nano-ZrO_2-containing samples at different cycles.

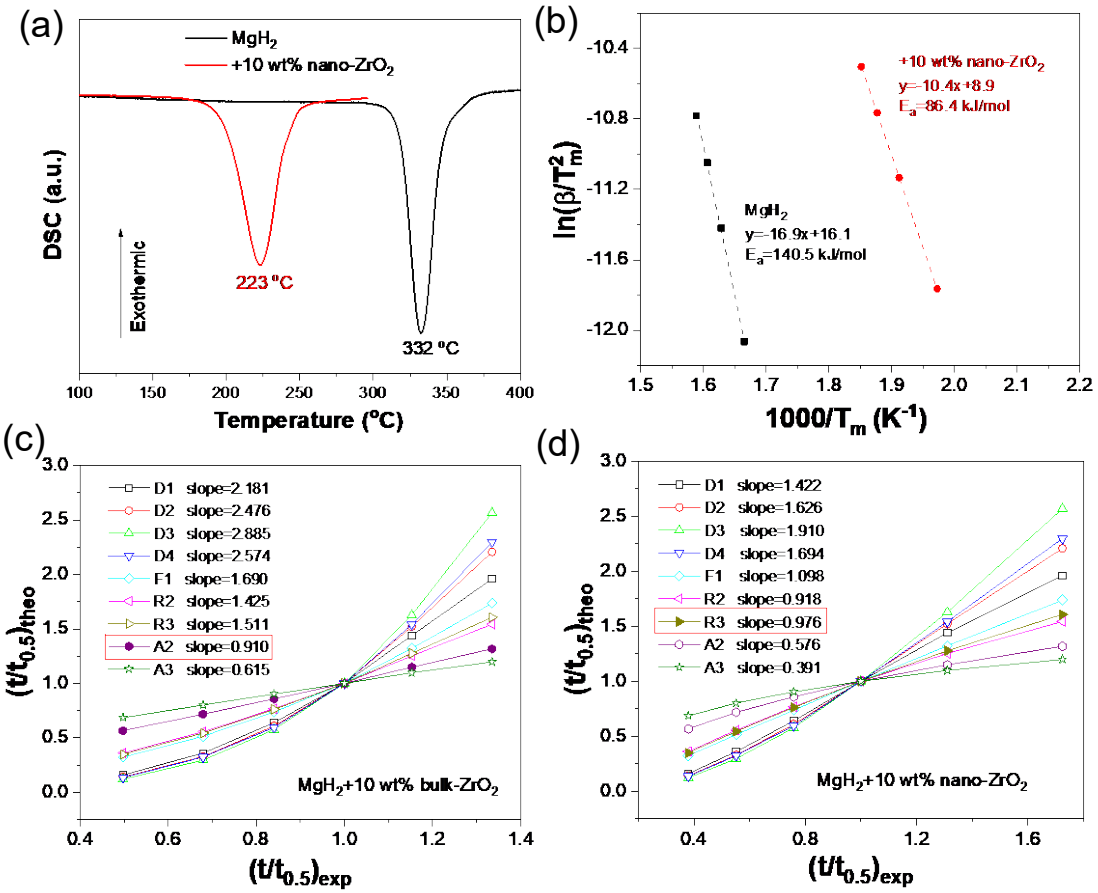

Fig. 8. (a) DSC curves and (b) Kissinger's plots of pristine MgH_2 and MgH_2+10 wt% nano-ZrO_2. The $(t/t_{0.5})_{theo}$ vs. $(t/t_{0.5})_{exp}$ for (c) MgH_2+10 wt% bulk ZrO_2 at 300 °C and (d) MgH_2+10 wt% nano-ZrO_2 at 260 °C using various kinetic models.

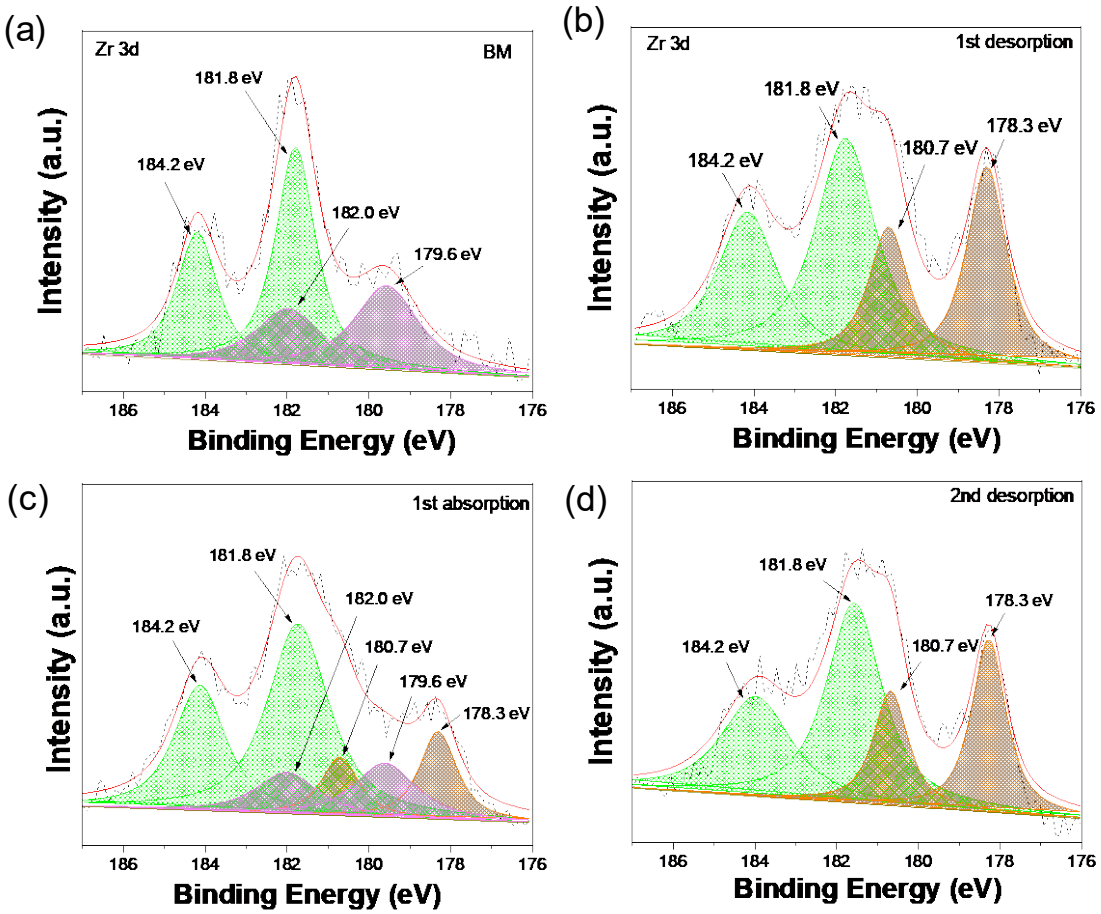

Fig. 9. High resolution XPS spectra of Zr 3d for MgH_2+10 wt% nano-ZrO_2 sample at different stages. (a) after milling, (b) after 1st desorption, (c) after 1st absorption and (d) after 2nd desorption.

Table 1 Hydrogenation kinetics of dehydrogenated MgH_2 doped with different catalysts under 50 bar H_2.

Temperature	Hydrogenation kinetics	
	nano-ZrO_2 (quantity-time)	**bulk ZrO_2 (quantity-time)**
50 ºC	1.8 wt%-60 s	0.45 wt%-20 min
100 ºC	4.0 wt%-12 s	1.0 wt%-20 min
150 ºC	5.2 wt%-6 s	3.1 wt%-20 min
200 ºC	5.9 wt%-6 s	4.9 wt%-20 min